## Energy materials

# Enhanced lithium storage capability enabled by metal nickel dotted NiO–graphene composites

Jin Chen[1] , Zhao Wang[1] , Jiechen Mu[1] , Bing Ai[1] , Tiezhu Zhang[1] , Wenqing Ge[1] , and Lipeng Zhang[1,*]

[1] School of Chemistry and Chemical Engineering, Shandong University of Technology, Zibo 255049, China

## ABSTRACT

The electrochemical performance of Li-ion batteries, which is limited by large volume changes and low intrinsic conductivity, can be improved by using a NiO–graphene composite as an electrode. Herein, we constructed metallic Ni-dotted NiO flakes on folded graphene and evaluated the electrochemical performance of the resulting composites. Introduction of graphene produced an excellent 2D structure that led to the homogeneous growth of Ni–NiO particles and improved the structural stability and conductivity of the final material. After 50 cycles, the reversible discharge capacity of Ni–NiO/G-2 reached 660.7 mAh g$^{-1}$ at a current density of 100 mAh g$^{-1}$ and approximately 75.0% of the capacity was maintained relative to the initial discharge capacity. The Ni–NiO/G-4 electrode displayed excellent high-rating performance, and the metallic Ni particles effectively improved the reversibility of solid electrolyte interface (SEI) films. Test results showed that the decomposition/regeneration of SEI films influenced the charge/discharge capacities of the electrodes during cycling.

## Introduction

Li-ion batteries (LIBs) have received considerable attention as promising energy storage devices. In the development of these batteries, the processes applied to prepare cathode materials are very mature, and studies on anode materials are expected to yield promising findings [1–3]. As commercialized materials, carbon anode materials present good electrochemical performance. Li atoms can intercalate graphite layers to form an intercalation compound during a cell's operation [4, 5]. This intercalation reaction prevents the deposition of metallic Li on graphite surfaces and dendritic growth [6]. However, this type of material is limited by several defects, such as low specific capacity (372 mAh g$^{-1}$), low initial coulombic efficiency, and co-intercalation between organic solvents and Li-ions. When used as active materials of LIBs, transition metal oxides show high specific capacities and retention rates [7, 8]. A number of these oxides, such as CoO [9, 10], FeO [11], NiO [12–14], CuO [15], and Fe$_3$O$_4$ [16, 17], can react with Li metal to form pure metal and reversible Li$_2$O.

🖄 Springer

These metal oxides typically present high specific capacities and high energy densities and can withstand high-power charging/discharging processes. However, most of them also exhibit poor electrical conductivity and structural collapse, especially during cyclic charging/discharging [18].

NiO has been extensively studied as an environment-friendly and inexpensive transition metal oxide; in particular, it displays excellent electrochemical performance as an anode material [19–23]. NiO has been synthesized into sphere-like [12], flower-like [24], and sheet structures [25], all of which have effectively relieved structural collapses during the electrochemical process. The capacity of NiO is significantly improved when it is compounded with other metal oxides, such as $SnO_2$ [26, 27] and $SiO_2$ [28]. When amorphous carbon is coated on NiO particles, the active material exhibits improved structural stability and rate performance. Graphene has become increasingly important in LIBs because of its extraordinary 2D structure and excellent electrical conductivity [3, 21, 22, 25]. Graphene provides large surface areas for loading NiO particles and can reduce the internal resistance of materials. Previous results reveal that the degree of graphitization of this composite increases after it is composited grapheme [3].

In this work, graphene is used to prepare high-performance NiO-based functional materials with improved electric conductivity and structural stability. The resulting 2D structure can effectively reduce the extent of pulverization and agglomeration, and metallic Ni, which is restored by graphene at high temperature, acts as an efficient catalyst that activates the electrochemical decomposition of electrolytes. This process further enhances the formation/decomposition of solid electrolyte interface (SEI) films and provides additional specific capacity.

# Experimental

## Synthesis of composites

Graphene oxide (GO) was synthesized from graphite powder (< 44 μm, Qingdao Black Dragon Graphite Co., Ltd., Shandong) via a modified Hummers method. The GO was collected by freeze-drying and reduced to graphene by a rapid thermal process at 500 °C under a $N_2$ (99.999%) atmosphere for 3 min.

Then, the as-prepared graphene was dispersed into a mixture containing 50 mL of deionized water and 50 mL of ethanol under 600 W ultrasonication for 30 min. The upper layer suspension was mixed with 0.5 g of $NiCl_2 \cdot 6H_2O$ (≥ 98.0%, Bodi Chemical Co., Ltd., Tianjin) and 0.25 g of NaOH (≥ 99.0%, Zhiyuan Chemical Reagent Co., Ltd., Tianjin) by magnetic stirring for 12 h. Thereafter, the suspension was transferred to a Teflon-lined stainless steel autoclave and maintained at 140 °C for 12 h. The products were rinsed several times with deionized water to remove foreign ions, and the obtained $Ni(OH)_2$/graphene was calcined at 450 °C under an $N_2$ (99.999%) atmosphere for 2 or 4 h in a tube furnace (GSL1600X) to form Ni–NiO/graphene; the resulting products were labeled as Ni–NiO/G-2 and Ni–NiO/G-4, respectively. Pure NiO was synthesized via the same procedure but without addition of graphene.

## Material characterization

The as-obtained samples were characterized by X-ray diffraction (XRD, Bruker AXS, D8 Advance), micro-Raman spectroscopy (RM, 1000-Invia), field-emission scanning electron microscopy (SEM, FEI, Sirion 200), and transmission electron microscopy (TEM, FEI, Tecnai G2F20 S-TWIN). Thermogravimetric (TG) measurement was performed using a thermogravimetric analyzer (STA, Netzsch STA 449) to confirm graphene contents.

## Electrochemical characterization

The working electrode was fabricated by mixing the active material, acetylene black, and polyvinylidene fluoride at a mass ratio of 8:1:1. The obtained slurry was coated onto a copper foil and then dried at 60 °C for 12 h. The electrodes were examined using 2032-type coins assembled in a glove box (Mikrouna, Super 1220). A cell was fabricated from an electrode, a polyethylene microporous membrane paper (Celgard 2400), Li foil, and electrolyte containing 1 M $LiPF_6$. Charge/discharge performances were tested using a LAND cell tester (CT2001A, LANHE) with different constant currents in the potential range of 0.01–3.0 V (vs. $Li/Li^+$) at room temperature. Cyclic voltammetry (CV) was performed on a CHI electrochemical workstation (CHI660D, China) at 0.5 mV $s^{-1}$ between 0.01 and 3.0 V (vs. $Li/Li^+$). Electrochemical impedance spectroscopy was

conducted on an IM6e electrochemical workstation (Zahner, Germany) over a frequency range of 0.01 Hz to 100 kHz and an alternating current modulation of 5 mV. The galvanostatic intermittent titration technique (GITT) was performed using the LAND cell tester. Prior to the GITT test, the cell was cycled five times at a current density of 100 mA g$^{-1}$.

## Results and discussion

### Structure, composition, and morphology of the composites

Figure 1a shows the diffraction peaks of Ni–NiO/G-2 and Ni–NiO/G-4. Peaks at 37.29°, 43.30°, 62.96°, 75.43°, and 79.36° (corresponding to the (111), (200), (220), (311), and (222) reflections, respectively) are consistent with the standard crystallographic data (JCPDS 78-0423) [29]; these results indicate that NiO has a nanocrystalline cubic structure. The diffraction peaks at 44.49°, 51.69°, and 76.35° (corresponding to the (111), (200), and (220) reflections, respectively) are in good agreement with JCPDS 70-1849 [29], thus implying that Ni has a face-centered cubic structure. The diffraction peak (002) of graphene is typically located at approximately 24°. However, this feature is not obvious in Fig. 1a because the graphene content of the composites was low and the diffraction of disorderly stacked graphene nanosheets is weaker than that of well-crystallized NiO and Ni. To confirm the existence of graphene, the Raman spectra of Ni–NiO/G-2 was obtained, as shown in Fig. 1b. No metallic Ni Raman peaks appear in this figure because of the absence of molecular vibrations among Ni atoms. The composite displays two sharp peaks at 1330 and 1594 cm$^{-1}$, which, respectively, correspond to the D and G bands of graphene [22]. In addition, a weak Raman peak is found at 545 cm$^{-1}$, which corresponds to the longitudinal optical phonon mode of NiO. Given that Ni particles can be easily oxidized in air, the graphene content of the Ni–NiO/graphene composites is difficult to confirm. The composition and the element bonding states of the Ni–NiO/G-4 samples were determined by XPS measurements, as can be seen from Fig. S1a. Results showed that the as-prepared composites were simply composed of the graphene and Ni-based materials. The Ni 2p peak of two samples can be deconvoluted into two components centered at 871.7 and 874.73 eV, can be well in
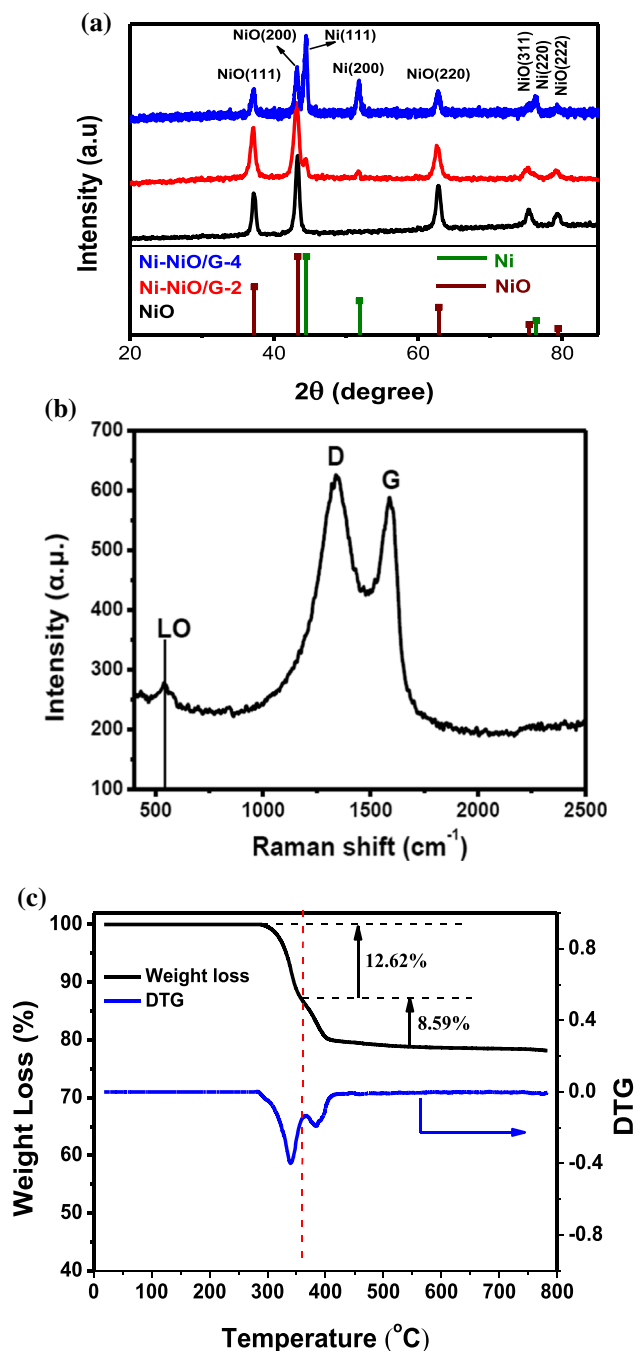


**Figure 1** XRD patterns of pure NiO, Ni–NiO/G-2 and Ni–NiO/G-4 composites (**a**); Raman spectra of the of Ni–NiO/G-2 composites (**b**); TG curve of Ni(OH)$_2$/graphene precursor (**c**).

agreement with the characteristic of Ni$^{2+}$ 2p and Ni species, respectively (see Fig. S1b) [30]. It is concluded that the presence of Ni in the Ni–NiO/G composites promotes an impressive electrochemical performances. Figure 1c illustrates the TG curves of the Ni(OH)$_2$/graphene precursor. The weight of the

material obviously drops by 21.21% from 290 °C to 400 °C. By comparison, the DTG curve presents two sharp peaks within the same temperature range. This phenomenon can be explained by the two weight-loss reactions corresponding to the dehydration of Ni(OH)$_2$ and the oxidation of graphene. The weight loss of the dehydration process from 290 °C to 360 °C is approximately 12.62%, and the weight loss of the oxidation process from 360 °C to 400 °C is approximately 8.59%. The TG measurement results showed the graphene content of precursor is approximately 8.59% and the content of Ni–NiO is 78.79%, as shown in Fig. 1c. The content of NiO in the total composite can be calculated by the XPS test (Fig. S1), which can confirm the content of Ni$^{2+}$. Results showed that the content of Ni, NiO, and graphene in this composite is 11.17, 67.62, and 8.59%, respectively.

The morphologies of the prepared materials were assessed by SEM and TEM. Field-emission SEM images of the composites are shown in Fig. 2. Figure 2a, b displays the morphologies of pure NiO at different magnifications. NiO particles aggregate into a large bulk after the same synthetic route, and a few hairline cracks are distributed on its surface at low magnification. The high-magnification photograph shows that the bulk materials are composed of agglomerated spherical particles with sizes in the range of 30–65 nm. Moreover, hairline cracks and micropores could be observed between agglomerated particles. This structure can provide the electrolyte and Li-ions pathways through which they can seep into the materials. Nevertheless, these pathways are blocked because of structural collapse during the cycling process. Thus, Li-ions cannot react with NiO particles within the bulk, and the capacity rapidly declines. Figure 2c, d and e, f display the microstructures of Ni–NiO/G-2 and Ni–NiO/G-4, respectively. The Ni–NiO/graphene composites present smaller particle sizes and laminated structures after introduction of graphene. Such a sheet structure can be infiltrated by electrolytes containing solvated Li-ions. With prolonged calcination, the size of the Ni–NiO/graphene composites decreases due to consumption of graphene-reducing NiO and its transformation into metallic Ni particles. The degree of dispersion is also significantly improved, although the graphene content decreases.

Figure 3 depicts the TEM images of Ni–NiO/G-2 and Ni–NiO/G-4. The Ni–NiO/graphene composites obtained are composed of different-sized nanosheets, as shown in Fig. 3a–d. The Ni–NiO nanosheets homogeneously grow on graphene to form a 2D structure, and no severe agglomeration occurs among the particles of the active material. Graphene prevents particles from forming a large block, and its excellent conductivity reduces the internal resistance of the system and significantly improves battery performance. The high-magnification TEM images reveal different fringe patterns and confirm the crystalline nature of the samples. The interplanar spacings measured from the fringe pattern are 0.204 and 0.24 nm, which correspond to the (111) planes of metallic Ni and NiO, respectively. This result is consistent with the XRD patterns illustrated in Fig. 1a.

## Electrochemical performance

Figure 4a–c shows results of the 1st, 2nd, 5th, and 10th charge–discharge cycle tests conducted on the NiO– and Ni–NiO/graphene-based materials in the range of 0.001–3.0 V at 100 mA g$^{-1}$. The first discharge capacity of NiO is 1059.3 mAh g$^{-1}$, and a voltage plateau appears at 0.75 V. This process may be attributed to the formation of both an SEI film and Li$_2$O. The first charge capacity is 798.6 mAh g$^{-1}$, which suggests that the irreversible capacity corresponding to the SEI film is 260.68 mAh g$^{-1}$. The second discharge capacity is 831.0 mAh g$^{-1}$, which greater than the first charge capacity by 32.4 mAh g$^{-1}$, likely because the SEI film is incompletely decomposed at 1.3 V during the first charge process and then repaired through consumption of Li in the next discharge process. The second charge capacity is 744.1 mAh g$^{-1}$, which corresponds to an irreversible capacity of 86.89 mAh g$^{-1}$. This finding may be ascribed to the collapse of the structure of NiO particles, which cannot endure the strong structural stress generated during the discharge/charge process. After 10 cycles, the discharge capacity gradually decays to 372.41 mAh g$^{-1}$, and the voltage plateaus at 1.0 and 2.2 V, which correspond to the intercalation and deintercalation processes of Li-ions, before gradually fading off. After 50 cycles, the plateaus nearly completely vanish, and the remaining capacity is 94.6 mAh g$^{-1}$. In Fig. 4b, the first discharge capacity of Ni–NiO/G-2 occurs at 1713.5 mAh g$^{-1}$, and the discharge voltage plateau increases to 0.75 V. These extended capacities are mainly due to the emergence of numerous

**Figure 2** The SEM images of pure NiO (**a**, **b**), Ni–NiO/G-2 (**c**, **d**) and Ni–NiO/G-4 (**e**, **f**).
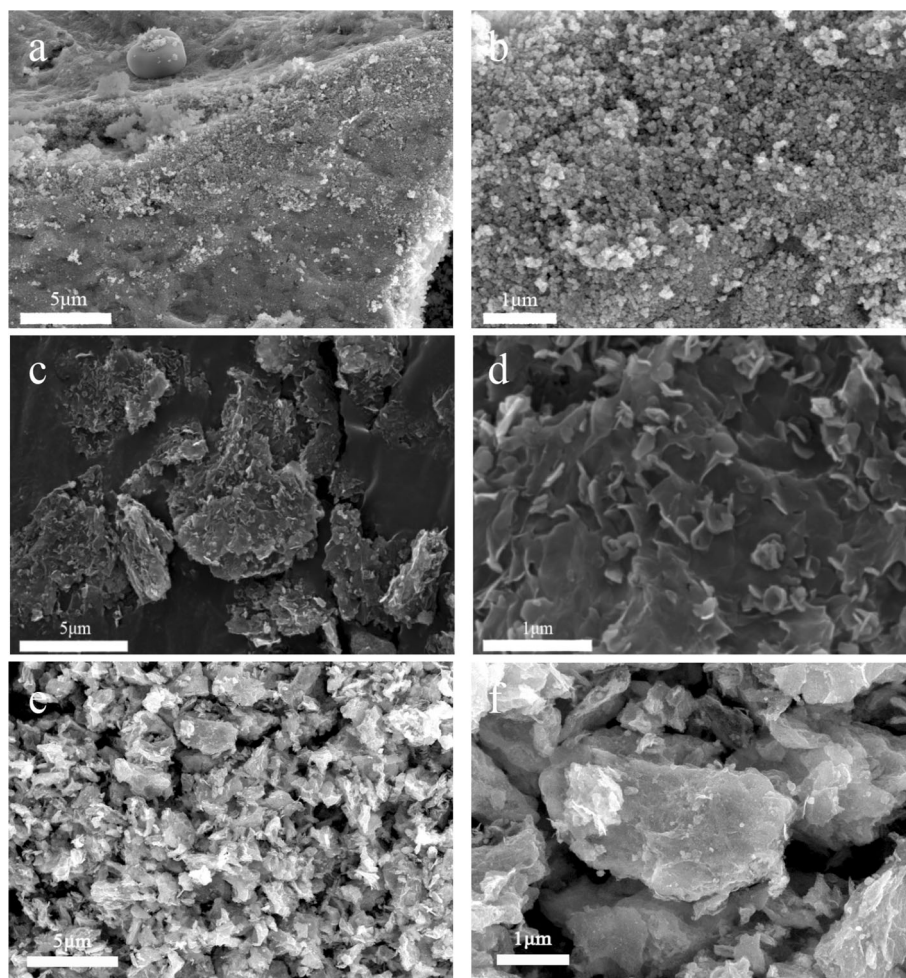


irreversible SEI films. The first charge capacity is 881.2 mAh g$^{-1}$, which was greater than that of pure NiO by 82.6 mAh g$^{-1}$. Some portions of NiO are reduced to metallic Ni by graphene under a N$_2$ atmosphere, and this material cannot be alloyed with Li metal to realize intercalation/deintercalation. Thus, another reaction probably occurs to accommodate the excess Li$^+$ in the system.

Graphene has a stable 2D structure and provides a stable base for the growth of NiO particles. Such a structure can effectively relieve structural collapse commonly observed during the electrochemical process. This phenomenon is reflected by the gradual reduction in voltage plateaus at 1.0, 2.2, and 1.3 V, although the discharge capacity remains at 826.3 mAh g$^{-1}$ after 10 cycles. Even after 50 cycles, the plateaus are still clearly visible, and the discharge capacity is maintained at 660.7 mAh g$^{-1}$. While the introduced graphene relieves the capacity loss during the electrochemical process, it cannot restrain the declining in electrode performance. The reduction degree of NiO is improved by prolonging the annealing time, and the electrochemical performance is illustrated in Fig. 4c. The first discharge capacity of Ni–NiO/G-4 is only 976.8 mAh g$^{-1}$, which is considerably lower than that of Ni–NiO/G-2, possible because the annealing process produces a large amount of metallic Ni, which cannot alloy with Li. The first charge capacity is 590.5 mAh g$^{-1}$, which corresponds to a coulombic efficiency of 60.5%. Moreover, the discharge platform returns to 0.5 V. After 50 cycles, the charge/discharge capacities are no longer diminished and remain at 556.9 mAh g$^{-1}$.

Figure 5 shows the voltage polarization and its variation as a function of the current of pure NiO– and Ni–NiO/G-based materials. In Fig. 5a, all electrodes were performed at 100 mAh g$^{-1}$; "0" on the x-axis refers to all delithiation states, and "1" corresponds to all intercalation states. The introduced graphene and metallic Ni do not influence the total
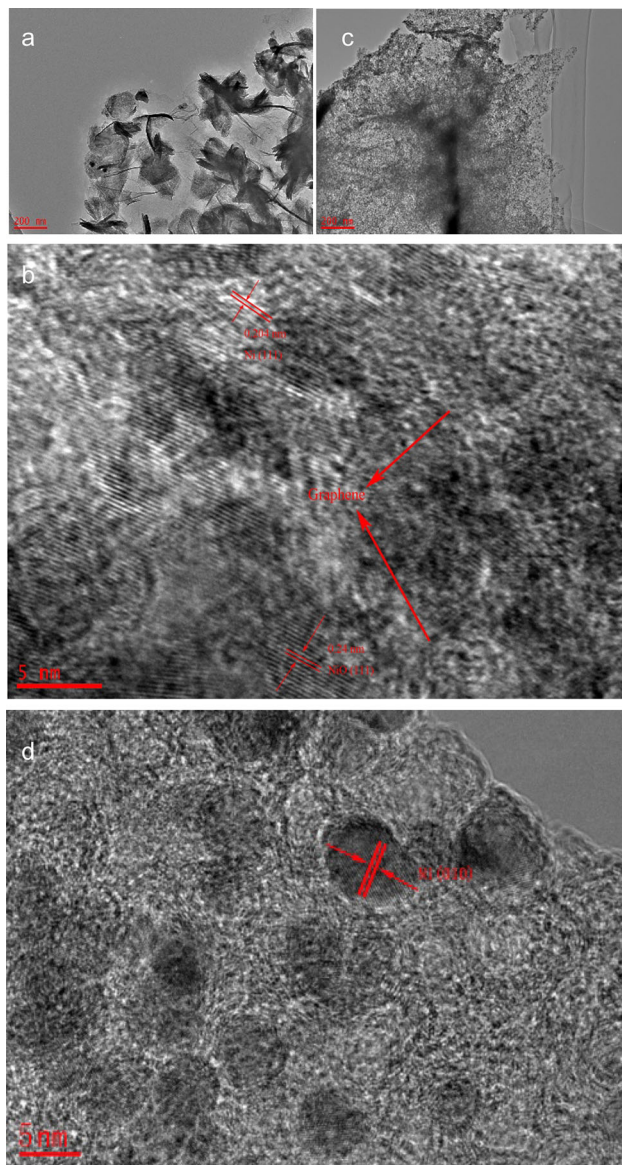
**Figure 3** The TEM images of Ni–NiO/G-2 (**a**, **b**) and Ni–NiO/G-4 (**c**, **d**).

voltage polarization, which ranges from 0.1 V to 1.5 V. This type of voltage polarization restricts the practical application of NiO-based materials. In general, the voltage polarization increases with increasing current density, and Fig. 5b reveals their functional relation in pure NiO– and Ni–NiO/G-based materials. The voltage polarization of different materials is linearly related to their current density. However, the slopes vary significantly when graphene and metallic Ni are introduced to NiO. The growth rate of the voltage polarization is reduced by enhancements in electrical conductivity.
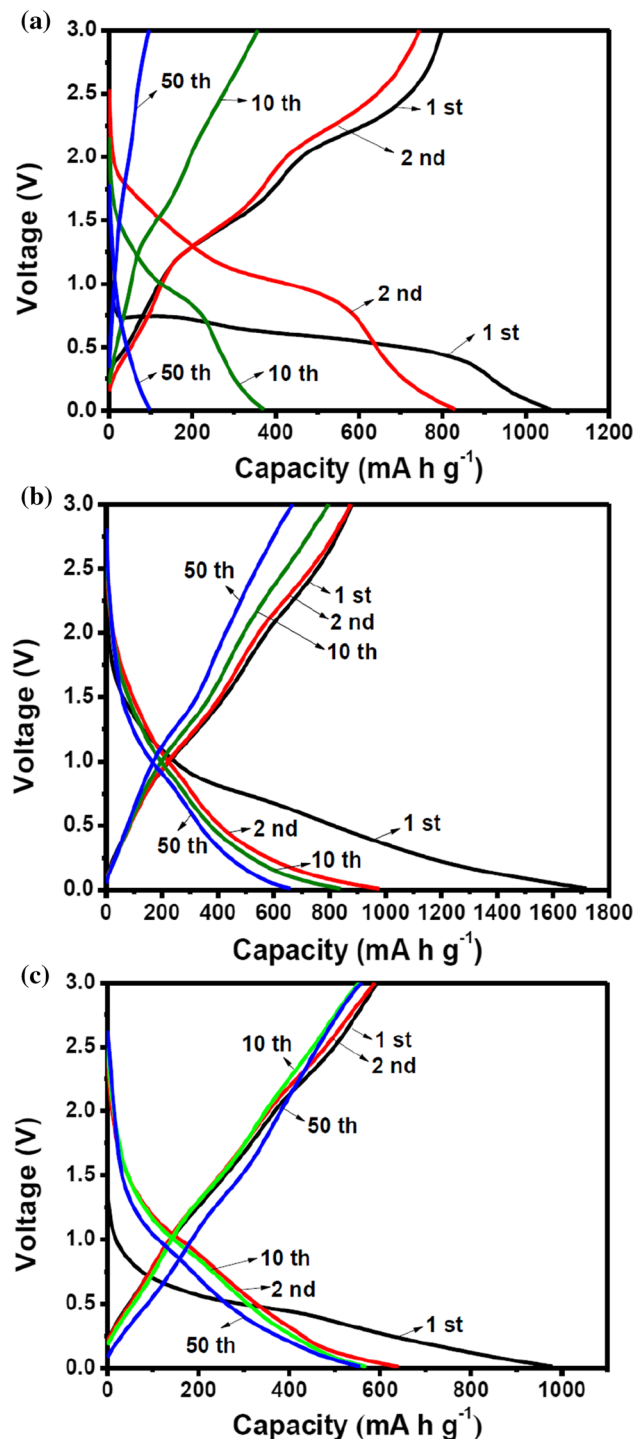


**Figure 4** Galvanostatic charge–discharge curves of **a** pure NiO, **b** Ni–NiO/G-2 and **c** Ni–NiO/G-4 composites at the 1st, 2nd 10th and 50th cycle.

Figure 6 illustrates the voltage polarizations of the Ni–NiO/G-4 electrode at different embedded Li states. The voltage difference does not significantly change during the discharge process and is
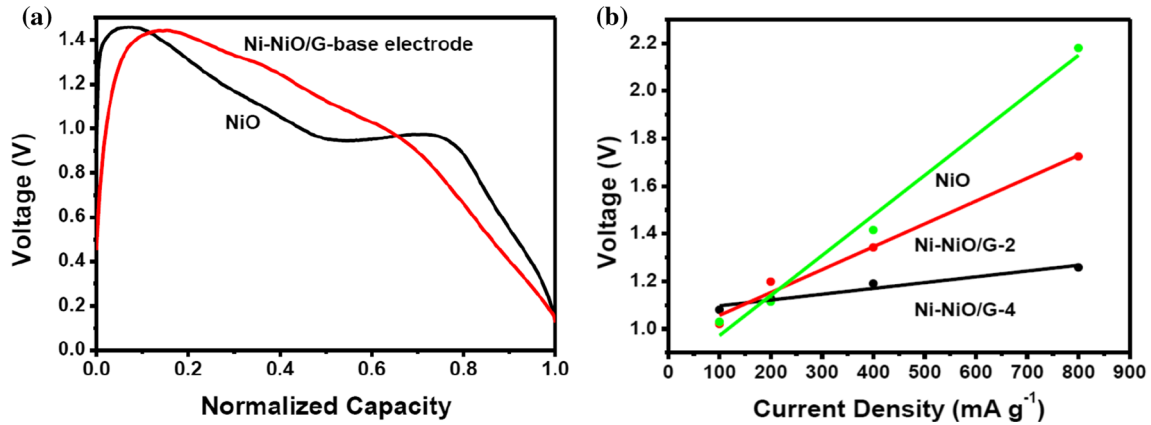
**Figure 5** Voltage polarization analysis (**a**) and the variation of voltage polarization as a function of current (**b**) about pure NiO and Ni–NiO/G base materials.

maintained at around 0.1 V. By contrast, the voltage polarization markedly changes during the charge process and reaches 0.45 V at all delithiation states. In the NiO-based materials, the electrode conductivity reaches 5000 S cm$^{-1}$ when two-thirds of the NiO is transformed into Ni particles. Thus, the electrical conductivity cannot restrict the reaction rate of electrodes during the discharge process. Ni particles gradually reacted with Li$_2$O to form a NiO semiconductor, and the reduced electrical conductivity gradually increases the voltage polarization.

CV was conducted to confirm the oxidation–reduction reactions of the electrode materials. In the first cycle, the three materials present strong reduction peaks at 0.397, 0.4, and 0.375 V, which confirms the formation of an SEI film and Li$_2$O. In the subsequent process, the first oxidation peaks appear at 1.44 and 1.36 V, thereby reflecting the decomposition of the SEI film [22, 30, 31]. The next oxidation peaks

appear at 2.26 and 2.25 V, which reflects the reaction between Ni and Li$_2$O. For pure NiO, two reduction peaks appear at 1.27 and 1.09 V (Fig. 7a), corresponding to the regeneration of the SEI film and the reaction between NiO and Li-ions. As shown in Fig. 7c, these two reduction peaks change to 1.5 and 0.9 V due to drastic Li-driven, structural, or textural modifications after doping with graphene [32]. Comparison of the two types of CV formations reveals reduction/oxidation peaks indicating the obvious decomposition/regeneration of the SEI film after production of metallic Ni. On the one hand, metallic Ni can catalyze the electrolyte decomposition reaction to promote the formation of the SEI film [29]. On the other hand, graphene-doped NiO has a highly ideal graphitized structure that generates a loose SEI film [6]. Thus, when charged to 1.0 V, SEI film decomposition is further intensified, and the regeneration peak at 1.55 V is enhanced. In addition,
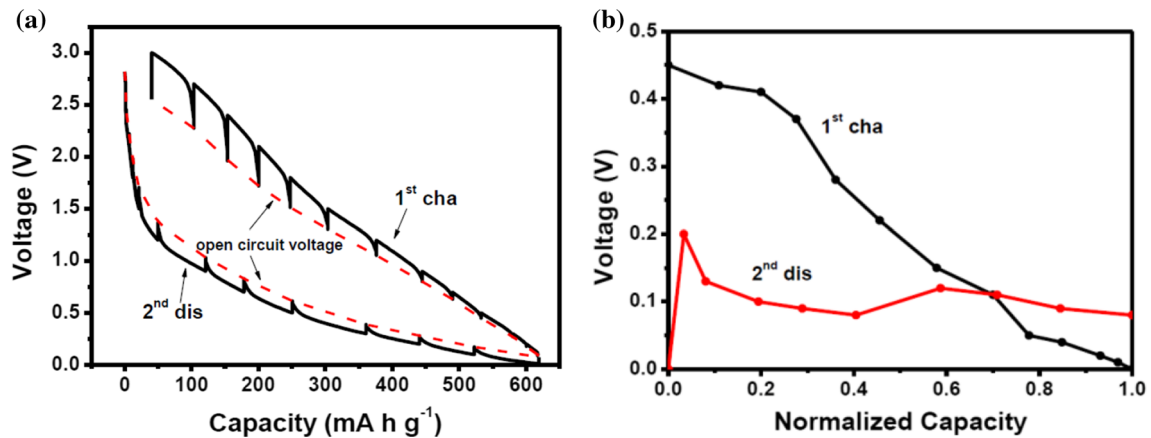


**Figure 6** The GITT curve (**a**) and voltage polarization value at different embedded lithium state (**b**) of Ni–NiO/G-4 electrode.
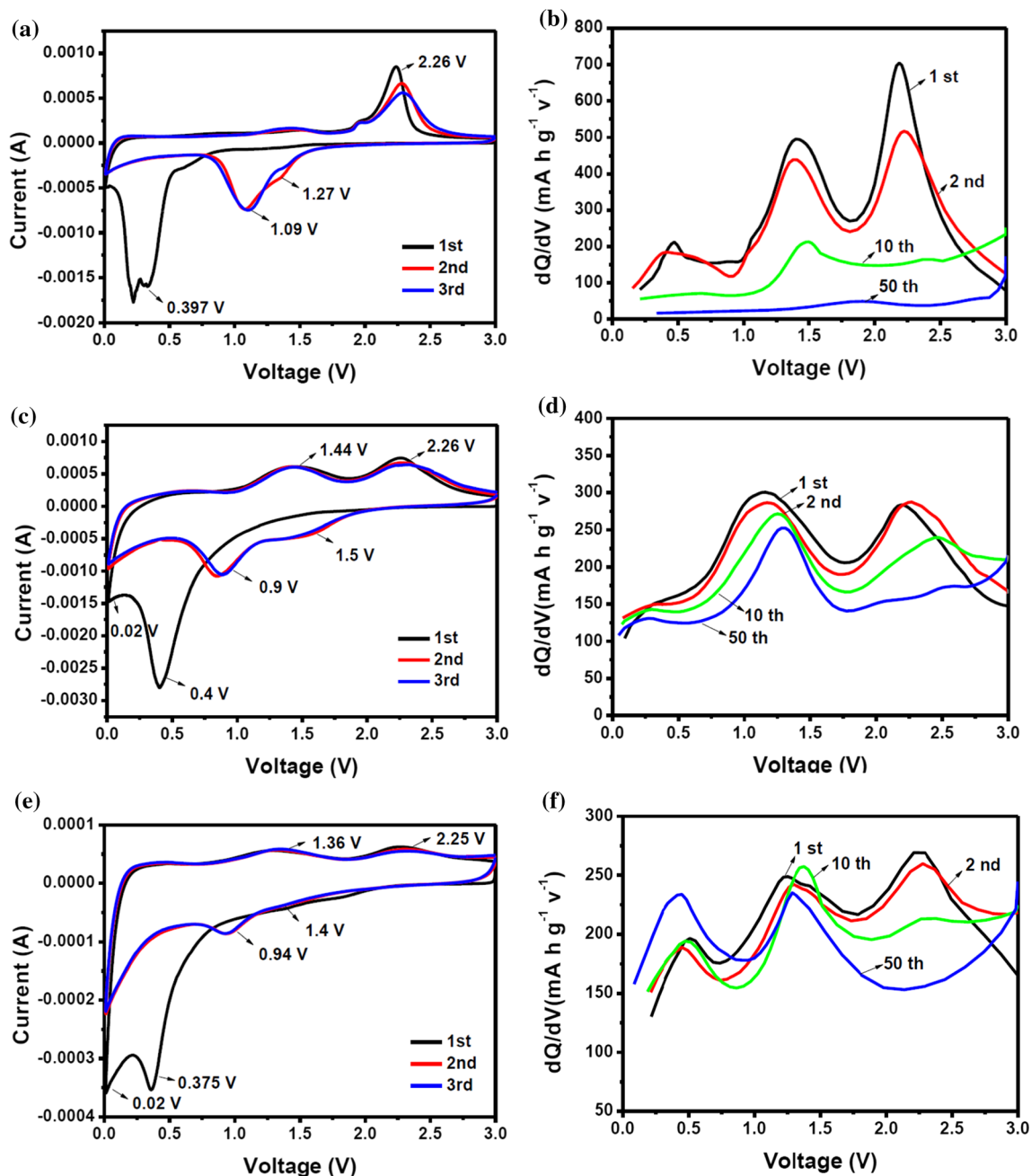
Figure 7 The CV curve and the differential capacity curve of pure NiO (**a**, **b**), Ni–NiO/G-2 (**c**, **d**) and Ni–NiO/G-4 (**e**, **f**).

Fig. 7e shows that the redox peaks corresponding to the reversible reaction between NiO and Li-ions are reduced with increasing calcining time.

To analyze the side reaction at 1.44 V, the differential capacity curves of the materials were obtained based on the charge/discharge curves of the different composites. In Fig. 7b, the peak intensity of pure NiO at 1.44 V gradually decays as the cycle number increases. After 50 cycles, the side reaction nearly

vanishes, indicating that disappearance of active sites promotes the decomposition of the SEI. For Ni–NiO/G-2 (Fig. 7d), the peak corresponding to the side reaction presents a slow decay, presumably due to the synergistic effect between the Ni particles and graphene. The decay trend is even slower for the Ni–NiO/G-4 electrode (Fig. 7f), probably because the improved content of Ni particles provides more

active sites for side reactions, which promote SEI decomposition.

In general, the Ni–NiO/graphene-based composites exhibit an irregular sheet structure that forms an unsound SEI film. The electrochemical process of the composites is illustrated in Fig. 8. Prior to the charge/discharge process, the synthesized materials display a flake structure, as shown in Fig. 8a. Then, SEI films are generated when discharged to 1.5 V, and the greatest degree is achieved at 0.35 V in the first cycle. As reported in a previous study, graphite has two characteristic surfaces: the surfaces parallel to the graphene layers are basal planes, and the surfaces normal to the graphene layers are edge planes [6]. SEI films are generated along these two planes, as shown in Fig. 8b. At the same time, Li-ions are embedded into NiO particles and cause a slight volume expansion. Moreover, the SEI films generated at the edge plane are relatively unstable and easily decomposed. In Fig. 8c, the SEI films generated at the edge planes begin to decompose when charged to 1.0 V. This reaction provides additional $Li^+$ to improve the capacity of the electrode. In the next cycles, the SEI films regenerate on the edge plane to form a dense film, as shown in Fig. 8d.

Comparison of the cycle performances of the three materials in Fig. 9a indicates that the specific capacity of pure NiO presents a continuous decreasing trend. This phenomenon is consistent with previous reports [33, 34]. After 50 cycles, the charge capacity

continually decreases from 798.6 mAh $g^{-1}$ to 94.6 mAh $g^{-1}$, which implies that the reversible Li storage capacity is only 11.8%. First, SEI regeneration consumes a large amount of irreversible Li salts. Second, continual dilatation and contraction of the active material results in structural collapse, which aggravates the loss of electrical contact between the active material and the current collector. The charge capacity the Ni–NiO/G-2 electrode is maintained at a stable condition; it declines after 5 cycles and slightly increases after 10 cycles. The charge capacity of this electrode decreases from 881.2 mAh $g^{-1}$ to 660.7 mAh $g^{-1}$, and its reversible Li storage capacity reaches 75.0% after 50 cycles. Besides its architectural stability, partial decomposition of the SEI films could contribute to the total charge capacity of this electrode, which is greater than that of previous pure NiO electrodes [29]. As shown in the CV curves, metallic Ni efficiently catalyzes the electrochemical decomposition of the electrolytes. The initial coulombic efficiencies of pure NiO and Ni–NiO/G-2 are 71.3% and 51.4%, respectively. This phenomenon could be attributed to the large specific surface area of graphene, which allows insertion of numerous Li-ions into its layers to promote the synthesis of the irreversible portion of SEI films. In addition, metallic Ni cannot store Li-ions. Thus, the equivalent capacity of Ni–NiO/graphene is less than that of pure NiO. The coulomb efficiency gradually increases and remains at 98% in subsequent cycles. The first charge



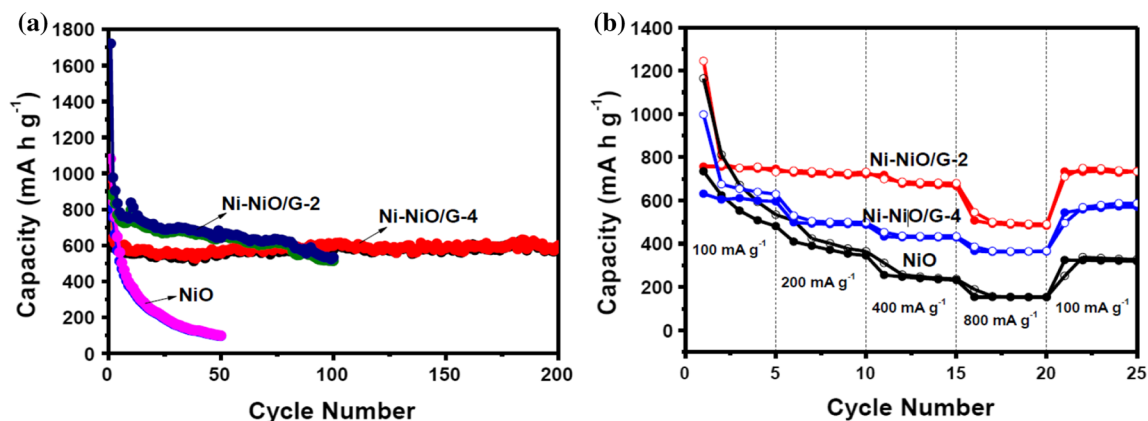**Figure 8** The simulated diagram of SEI films transformation.

(a)

(b)

Discharge

Charge

(d)

(c)

Discharge
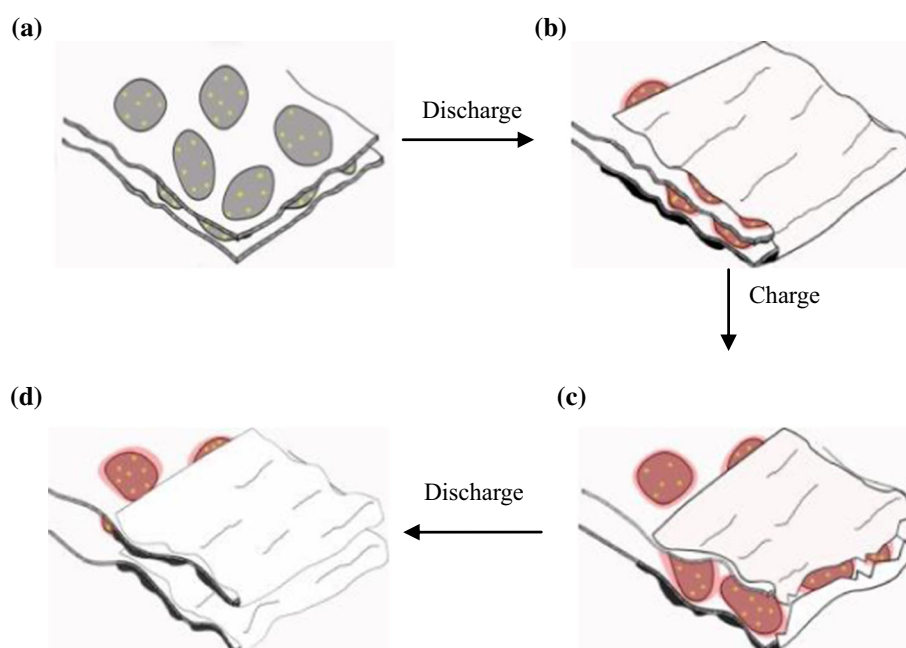
**Figure 9** The cycling performance and coulombic efficiency at 100 mA g$^{-1}$ (**a**) and the rate performance at different rates (**b**) of pure NiO and Ni–NiO/graphene composites.

capacity of the Ni–NiO/G-4 electrode is only 593.6 mAh g$^{-1}$, which is substantially lower than those of the pure NiO and Ni–NiO/G-2 composites. Moreover, its capacity is maintained at 594.8 mAh g$^{-1}$ even after 200 cycles. This phenomenon reveals that Ni–NiO/G-4 has a cycling performance superior to those of the other materials. Such excellent performance could be explained by an increase in active particles, which enhances the reversible decomposition of SEI films.

The Ni–NiO/graphene-based composites show markedly improved rate performance compared with pure NiO, as shown in Fig. 9b. The first specific charge capacity of pure NiO is 734.7 mAh g$^{-1}$ at a current density of 100 mA g$^{-1}$, and first charge capacities of approximately 409.9, 255.4, and 153.7 mAh g$^{-1}$ are obtained at current densities of 200, 400, and 800 mA g$^{-1}$, respectively. Only 55.8, 34.8, and 20.9% of the first charge capacity is retained at the fifth cycle under the same test conditions. When the current rate is returned to 100 mA g$^{-1}$, the electrode maintains a capacity of only 324.4 mAh g$^{-1}$ after 20 cycles at various current densities. The first charge capacities of the Ni–NiO/G-2 composite are 768.4, 735.4, 675.6, and 506.5 mAh g$^{-1}$ at current densities of 100, 200, 400, and 800 mA g$^{-1}$, respectively; thus, this composite demonstrates a high degree of reversibility. Moreover, the capacity of the composite recovers to 744.8 mAh g$^{-1}$ after cycling at different high rates, thus confirming its excellent rate capability. The Ni–NiO/G-4 electrode also demonstrated excellent rate performance. Besides its architectural stability, the enhanced electric conductivity of the material effectively improves the rate

performance of this electrode by releasing the voltage delay occurring at high rates.

To examine the change process of the SEI films during cycling, the Ni–NiO/G-4 cell was measured at the 1st, 10th, and 50th cycles, as shown in Fig. 10a. Figure 10b shows the high-frequency region of this material. The straight lines appearing in the low-frequency range, which correspond to the Warburg impedance (Ws), are close to the vertical axis from the 1st to the 50th cycle, thereby suggesting that the internal structure of the active materials is gradually stabilized. An equivalent electric circuit is shown in the inset in Fig. 10b. The high-frequency intercepts represent the electronic resistance in the electrolyte, which is presented as the equivalent series resistance ($R_S$) [35]. The diameters of the semicircle represent the resistance due to the SEI films ($R_{SEI}$) and the charge-transfer or reaction resistance ($R_{CT}$) [36]. As shown in Table 1, $R_{SEI}$ decreases from 8.383 Ω to 3.804 Ω, indicating that the SEI film decomposes to some extent from the 1st to the 10th cycle. However, $R_{SEI}$ increases from 8.383 Ω to 17.98 Ω as the number of cycles is increased from 1 to 50, thus indicating that the SEI films are gradually regenerated throughout the charge/discharge process.

## Conclusions

Ni–NiO/graphene-based composites were successfully synthesized by a traditional hydrothermal method and studied using different characterization methods. Ni–NiO particles homogeneously grew on graphene to form a sheet structure, which prevented
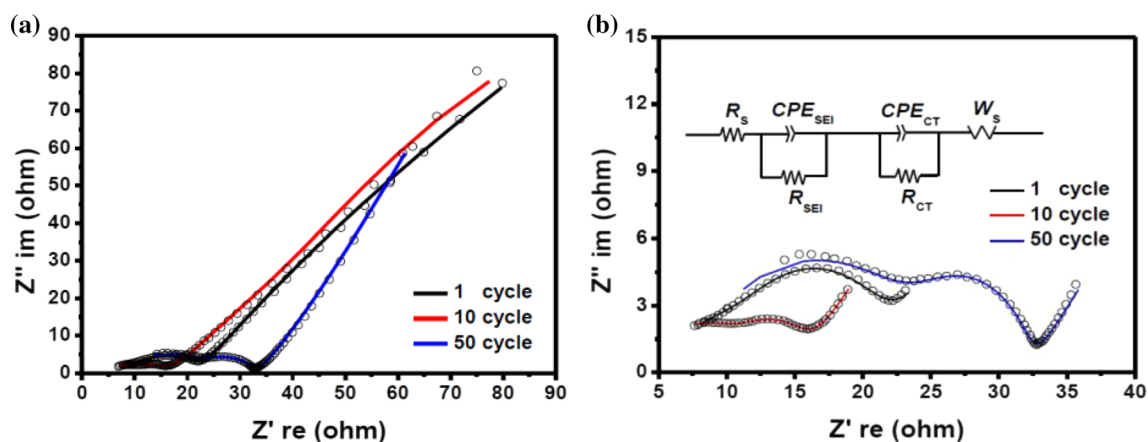
**Figure 10** The EIS curve (**a**) of Ni–NiO/G-4 composites; magnification of the curve and equivalent electric circuit (**b**) of Ni–NiO/G-4 composites.

**Table 1** The circuits fitting data of Ni–NiO/G-4 composites

| Cycle number | $R_S$ (Ω) | $R_{SEI}$ (Ω) | $R_{CT}$ (Ω) |
|---|---|---|---|
| 1 | 4.626 | 8.383 | 7.975 |
| 10 | 3.815 | 3.804 | 7.856 |
| 50 | 7.02 | 17.98 | 7.195 |

particles from forming large blocks. The excellent conductivity of graphene reduced the internal resistance and improved the electrochemical performance of the materials. Loose SEI films generated on the basal and edge planes of the active materials easily decomposed, and metallic Ni effectively improved the decomposition process of the electrolytes. The synergistic effects produced by Ni and graphene promoted the decomposition/regeneration of SEI films and improved the specific capacity of the composites.

**Electronic supplementary material:** The online version of this article (https://doi.org/10.1007/s10853-018-2882-3) contains supplementary material, which is available to authorized users.

## References

[1] Lv C, Yang X, Umar A, Xia Y, Jia Y, Shang L, Zhang T, Yang D (2015) Architecture-controlled synthesis of $M_xO_y$ (M = Ni, Fe, Cu) microfibres from seaweed biomass for high performance lithium ion battery anodes. J Mater Chem A 3:22708–22715

[2] Lv Y, Chen B, Zhao N, Shi C, He C, Li J, Liu E (2016) Interfacial effect on the electrochemical properties of the layered graphene/metal sulfide composites as anode materials for Li-ion batteries. Surf Sci 651:10–15

[3] Zhu T, Li X, Zhang Y, Yuan M, Sun Z, Ma S, Li H, Sun G (2018) Three-dimensional reticular material NiO/Ni–graphene foam as cathode catalyst for high capacity lithium–oxygen battery. J Electroanal Chem 823:73–79

[4] Rachid Y (1999) Surface chemistry and lithium storage capability of the graphite–lithium electrode. Electrochim Acta 45:87–97

[5] Liu L, Yang X, Lv C, Zhu A, Zhu X, Guo S, Chen C, Yang D (2016) Seaweed-derived route to $Fe_2O_3$ hollow nanoparticles/N-doped graphene aerogels with high lithium ion storage performance. ACS Appl Mater Interfaces 8:7047–7053

[6] An SJ, Li J, Daniel C, Mohanty D, Nagpure S, Wood DL (2016) The state of understanding of the lithium-ion-battery graphite solid electrolyte interphase (SEI) and its relationship to formation cycling. Carbon 105:52–76

[7] Sun J, Lv C, Lv F, Chen S, Li D, Guo Z, Han W, Yang D, Guo S (2017) Tuning the shell number of multishelled metal oxide hollow fibers for optimized lithium-ion storage. ACS Nano 11:6186–6193

[8] Li D, Yang D, Zhu X, Jing D, Xia Y, Ji Q, Cai R, Li H, Che Y (2014) Simple pyrolysis of cobalt alginate fibres into $Co_3O_4$/C nano/microstructures for a high performance lithium ion battery anode. J Mater Chem A 2:18761–18766

[9] Yuan W, Zhang J, Xie D, Dong Z, Su Q, Du G (2013) Porous CoO/C polyhedra as anode material for Li-ion batteries. Electrochim Acta 108:506–511

[10] Qiao H, Xiao L, Zheng Z, Liu H, Jia F, Zhang L (2008) One-pot synthesis of CoO/C hybrid microspheres as anode materials for lithium-ion batteries. J Power Sources 185:486–491

[11] Li X, Lin KW, Liang HT, Hsu HF, Galkin NG, Wroczynskyj Y, van Lierop J, Pong PWT (2015) The effects of interfacial interactions between Fe–O and Fe–Si induced by ion-beam bombardment on the magnetic properties of Si-oxide/Fe bilayers. Nucl Instrum Methods Phys Res Sect B 365:196–201

[12] Lin P, She Q, Hong B, Liu X, Shi Y, Shi Z, Zheng M, Dong Q (2010) The nickel oxide/CNT composites with high capacitance for supercapacitor. J Electrochem Soc 157:A818–A823

[13] Thi TV, Rai AK, Gim J, Kim J (2015) High performance of Co-doped NiO nanoparticle anode material for rechargeable lithium ion batteries. J Power Sources 292:23–30

[14] Palmieri A, Wang T, Zhang J, Spinner N, Liu M, Mustaina WE (2017) Modeling nickel oxide particle stress behavior induced by lithiation using a FEM linear elastic approach. J Electrochem Soc 164:A867–A873

[15] Hu Z, Liu H (2015) Three-dimensional CuO microflowers as anode materials for Li-ion batteries. Ceram Int 41:8257–8260

[16] Wan Y, Yang Z, Xiong G, Guo R, Liu Z, Luo H (2015) Anchoring $Fe_3O_4$ nanoparticles on three-dimensional carbon nanofibers toward flexible high-performance anodes for lithium-ion batteries. J Power Sources 294:414–419

[17] Wang L, Yu Y, Chen PC, Zhang DW, Chen CH (2008) Electrospinning synthesis of C/$Fe_3O_4$ composite nanofibers and their application for high performance lithium-ion batteries. J Power Sources 183:717–723

[18] Huang XH, Tu JP, Zhang CQ, Xiang JY (2007) Net-structured NiO–C nanocomposite as Li-intercalation electrode material. Electrochem Commun 9:1180–1184

[19] Lee DH, Kim JC, Shim HW, Kim DW (2014) Highly reversible Li storage in hybrid NiO/Ni/graphene nanocomposites prepared by an electrical wire explosion process. ACS Appl Mater Interfaces 6:137–142

[20] Su X, Chai H, Jia D, Bao S, Zhou W, Zhou M (2013) Effective microwave-assisted synthesis of graphene nanosheets/NiO composite for high-performance supercapacitors. New J Chem 37:439–443

[21] Li D, Yang D, Yang X, Wang Y, Guo Z, Xia Y, Sun S, Guo S (2016) Double-helix structure in carrageenan-metal hydrogels: a general approach to porous metal sulfides/carbon aerogels with excellent sodium-ion storage. Angew Chem Int Ed 55:1–5

[22] Zhou G, Wang DW, Yin LC, Li N, Li F, Cheng HM (2012) Oxygen bridges between NiO nanosheets and graphene for improvement of lithium storage. ACS Nano 6:3214–3223

[23] Vaidya S, Ramanujachary KV, Lofland SE, Ganguli AK (2009) Synthesis of homogeneous $NiO@SiO_2$ core–shell nanostructures and the effect of shell thickness on the magnetic properties. Cryst Growth Des 9:1666–1670

[24] Mollamahale YB, Liu Z, Zhen Y, Tian ZQ, Hosseini D, Chen L, Shen PK (2016) Simple fabrication of porous NiO nanoflowers: growth mechanism, shape evolution and their application into Li-ion batteries. Int J Hydrogen Energy 42:7202–7211

[25] Hwang SG, Kim G, Yun SR, Ryu KS (2012) NiO nanoparticles with plate structure grown on graphene as fast charge–discharge anode material for lithium ion batteries. Electrochim Acta 78:406–411

[26] Xing LL, Cui CX, He B, Nie YX, Deng P, Xue XY (2013) $SnO_2$/NiO core–shell nanobelts and their high reversible lithium storage capacity arising from synergisticeffect. Mater Lett 96:158–161

[27] Ju D, Xu H, Xu Q, Gong H, Qiu Z, Guo J, Zhang J, Cao B (2015) High triethylamine-sensing properties of NiO/$SnO_2$ hollow sphere P-N heterojunction sensors. Sens Actuators B Chem 215:39–44

[28] Ali AM, Najmy R (2013) Structural optical and photocatalytic properties of NiO–$SiO_2$ nanocomposites prepared by sol–gel technique. Catal Today 208:2–6

[29] Sun X, Si W, Liu X, Deng J, Xi L, Liu L, Yan C, Schmidt OG (2014) Multifunctional Ni/NiO hybrid nanomembranes as anode materials for high-rate Li-ion batteries. Nano Energy 9:168–175

[30] Luo Y, Weng M, Zheng J, Zhang Q, Xu B, Song S, Shen Y, Lin Y, Pan F, Nan C (2018) The origin of cycling enhanced capacity of Ni/NiO species confined on nitrogen doped carbon nanotubes for lithium-ion battery anodes. J Alloy Compd 750:17–22

[31] Ding C, Zhou W, Wang X, Shi B, Wang D, Zhou P, Wen G (2018) Hybrid aerogel-derived carbon/porous reduced graphene oxide dual-functionalized NiO for high-performance lithium storage. Chem Eng J 332:479–485

[32] Sun X, Yan C, Chen Y, Si W, Deng J, Oswald S, Liu L, Schmidt OG (2014) Three-dimensionally "curved" NiO nanomembranes as ultrahigh rate capability anodes for Li-ion batteries with long cycle lifetimes. Adv Energy Mater 4:1300912–1300917

[33] Yao WL, Wang JL, Yang J, Du GD (2008) Novel carbon nanofiber-cobalt oxide composites for lithium storage with large capacity and high reversibility. J Power Sources 176:369–372

[34] Yao W, Yang J, Wang J, Tao L (2008) Synthesis and electrochemical performance of carbon nanofiber–cobalt oxide composites. Electrochim Acta 53:7326–7330

[35] Bell J, Ye R, Ahmed K, Liu C, Ozkan M, Ozkan CS (2015) Free-standing Ni–NiO nanofiber cloth anode for high capacity and high rate Li-ion batteries. Nano Energy 18:47–56

[36] Wang W, Ruiz I, Ahmed K, Bay HH, George AS, Wang J, Butler J, Ozkan M, Ozkan CS (2014) Silicon decorated cone shaped carbon nanotube clusters for lithium ion battery anodes. Small 10:3389–3396